Optimization of continuous micromagnetic separation for the treatment of *Acinetobacter baumannii* bacteremia

By

Stephen Neil Petty Valenzuela

Thesis

Submitted to the Faculty of the

Graduate School of Vanderbilt University

in partial fulfillment of the requirements

for the degree of

MASTER OF SCIENCE

in

Biomedical Engineering

May, 2017

Nashville, Tennessee

Approved: Date:

Todd D. Giorgio, Ph.D.

Frederick R. Haselton, Ph.D.

ACKNOWLEDGMENTS

I would first like to thank Dr. Todd D. Giorgio for accepting me into his lab at Vanderbilt University and providing guidance in my research. Without his continued efforts to promote my education, I would not have been able to accomplish this. I would also like to especially thank Dr. Charleson S. Bell and Dr. Sinead E. Miller for providing the very foundations of my research and for their continual mentorship and assistance. Many thanks to Candace Grisham as well for assisting me as part of her undergraduate research. Thanks to the Giorgio lab for their support and friendship over the course of my career. I would also like to express my immense gratitude to David Schaffer, Clayton Britt, and the VIIBRE Microfabrication Core, as well as Dr. Haoxiang Luo for their assistance with this project. I thank my loving friends and family for supporting me throughout this process. Finally, I would like to thank the Department of Defense (DoD) (W81XWH-13-1-0397) and the Vanderbilt Undergraduate Summer Research Program for providing financial support for this work.

TABLE OF CONTENTS

Page

LIST OF TABLES

LIST OF FIGURES

CHAPTER 1

Bacteremia, sepsis, and their current diagnostic and treatment methods

1.1. Bacteremia and sepsis

Bacterial infections are common in all demographics and are present globally. In immunonormal cases, the infection is typically limited to a local site and is effectively suppressed by the immune system. However, with an impaired immune response, free bacteria can circulate in the bloodstream, resulting in bacteremia. From there, the infection can colonize other tissues. The abnormal immune response to these distributed bacteria or their toxins can result in life-threatening organ dysfunction, which is known as bacterial sepsis [1]–[3]. If not properly treated, sepsis can quickly progress into severe sepsis, septic shock, or death. Even after treatment, long-term outcomes include recidivism, recurrent or persistent organ dysfunction, or cognitive and functional impairment [4], [5].

In the United States, more than a million cases of severe sepsis are diagnosed annually [6]. With a mortality estimated between 28 and 50 percent [7], [8], severe sepsis is the tenth leading cause of death [8], exceeding the number of deaths from prostate cancer, breast cancer, and AIDS combined [9]. Furthermore, the incidence of sepsis is increasing in excess of population growth in developed countries [8]. Immunocompromised patients are especially susceptible to sepsis including the elderly, neonates, and hospitalized patients. Approximately half of severe sepsis cases occur in patients already in the ICU [10], and these infections are eight times as likely to result in death when compared with other diagnoses [6], incurring additional annual healthcare costs of more than $17 billion [7].

1.2. Diagnostic methods

Beyond the simple definition, there is no single definitive diagnosis for bacterial sepsis [2]. Symptoms resultant from an immune response are heterogeneous across patients and can range from fever or hypothermia, leukocytosis or leukopenia, tachycardia, and hypotension, none of which are unique to sepsis [2]. Certain innate biomarkers can be used as part of diagnosis, such as elevated lactate levels, inflammatory cytokines, C-reactive proteins, and procalcitonin, but these cannot differentiate between pathogen genera or species and primarily serve as a means of ruling out infection rather than confirmation of infection [9], [11], [12]. The only clinical means of determining the origin of sepsis – and thus the treatment – is the confirmation and identification of pathogens.

The "gold-standard" for pathogen identification is through blood culture [13]. Blood samples are aliquoted and cultured on selective media and incubated, enabling biological amplification and isolation of the pathogen. Some automation can be achieved by detecting growth via changes in partial pressures of gasses or changes in turbidity of liquid media. Differential staining (e.g., Gram staining) and other biochemical assays can also be used to classify the pathogen. However, these techniques are reliant on culturing, which require overnight incubation or longer, delaying effective treatment from being administered. Additionally, identification using these methods requires a technician, making pathogen identification outside of a hospital setting difficult. More sophisticated techniques such as polymerase chain reaction (PCR) and mass spectroscopy are being developed, but also currently suffer from the need for pathogen amplification and isolation to generate a bacteria-specific signal of sufficient quality to distinguish in comparison with the background of uninfected whole blood [14].

1.3. Treatment methods

Effective treatment of bacteremia involves elimination of bacteria at the source of infection. However, infections from blood-borne pathogens are inherently difficult to treat due to their spread from an initial site to other locations via the bloodstream; more specifically, the lungs, the liver, and the spleen suffer some of the greatest burden in bacteremia [11], [15]–[18]. Upon suspicion of sepsis, broad-spectrum antibiotics are administered as the standard of care, along with methods to stabilize the patient using intravenous fluids and oxygen, for example. Additional stabilization such as mechanical ventilation and kidney dialysis may be necessary for severely septic patients. After pathogen identification and antimicrobial susceptibility testing, a more specific antibiotic can be used. Administering an effective antibiotic within the first hour after hypotension increases the survival rate of patients significantly. However, only half of septic patients receive the appropriate therapy within the first six hours; each hour of delay decreases the chances of survival by 7.6% [19]. Antimicrobial treatment also has the potential to cause harm to patients by eliminating parts of the innate microbiome, especially in the gut, leading to various metabolic, immunological, and developmental disorders [20]. Further complicating sepsis treatment is the rise of multidrug resistant (MDR) pathogens. Pathogens that survive incomplete or ineffective treatment can pass on traits for antimicrobial resistance. These strains can then spread rapidly through a population, especially in hospital settings, resulting in increasing costs of treatment [21]. An increasing number of MDR strains and the diminishing number of new antimicrobials has prompted health organizations to classify combatting antimicrobial resistance as high priority [22], [23].

1.4. Acinetobacter baumannii infections

Acinetobacter baumannii, a Gram-negative bacterium, is of particular interest in sepsis pathology due to its hardiness: the bacterium can survive under extreme temperature, humidity, and pH conditions. As such, *A. baumannii* is found in a variety of geographic areas, including desert climates, and on numerous surfaces, including human skin, mucous membranes, and metal hospital bed rails [24]–[26]. Nosocomial *A. baumannii* infections are of increasing concern due to persistent emerging MDR strains, epidemiologically-complex outbreaks, and relatively high fatality rates, prompting the Centers for Disease Control and Prevention (CDC) to label MDR *Acinetobacter spp.* as a serious threat [22], [24]–[30]. To combat MDR *A. baumannii* and other MDR Gram-negative bacteria, colistin is the drug of choice. A polycationic decapeptide, colistin interacts with the lipopolysaccharides (LPS) in the bacterial outer membrane, destabilizing it and leading to cell death [31]. However, colistin was abandoned due to nephrotoxicity, ototoxicity, and neurotoxicity concerns; therefore, it is used only as an antibiotic of last resort. Unfortunately, strains of *A. baumannii* are developing resistance to colistin and similar antibiotics, further limiting treatment options [32].

1.5. Continuous micromagnetic separation

Continuous micromagnetic separation is a promising avenue of diagnosis and treatment of various bloodborne conditions. With these systems, magnetic nano- or microparticles bind to the cells or molecules of interest and are drawn out of flowing fluid with a strong magnetic gradient. This isolation can either serve as an isolation/amplification for diagnostic tests or as a treatment mechanism for itself. For example, systems have been developed to extract rare circulating tumor cells from blood samples [33] or for capture of bacteria from food samples [34]. However,

significant focus has been on extracorporeal blood cleansing of pathogens and toxins, similar to dialysis. With these devices, blood is withdrawn and mixed with magnetic (usually paramagnetic or superparamagnetic) particles, extracted with an extracorporeal magnetic separator, and returned to the patient; this has been shown to be efficacious in treating rats challenged with large doses of bacteria and endotoxin [35]–[38]. However, no device has been scaled up to treat humans as of yet.

1.6. Specific aims

In this work, the optimization of a microfluidic device for micromagnetic separation is outlined. First, the design and fabrication of microfluidic devices are described in Chapter 2. These devices are analyzed using computational fluid dynamics in Chapter 3. Then, the magnetostatic properties necessary for separation are determined in Chapter 4. In Chapter 5, a physically and physiologically-based pharmacokinetic separation model is used to justify the various parameters for an extracorporeal separation device. Finally, Chapter 6 discusses the potential future directions for extracorporeal separation.

CHAPTER 2

Microfluidic device design and fabrication

2.1. Introduction

Given the physical size of bacteria and the characteristics of magnetic forces, microfluidics techniques are necessary for continuous separation. Microfluidics are loosely defined as devices whose characteristic lengths are on the micrometer scale. With such small dimensions, extremely precise control of nanoliter or even picoliter volumes is possible. Microfluidic devices are also characterized by low Reynolds numbers, indicating a dominance of viscous forces over inertial forces. Fluid in this regime is well-characterized, exhibiting properties such as laminar flow and diffusion-limited transport. Cells can therefore be readily manipulated in this environment without incurring damage.

The concept of sheath flow is central to magnetic separation design. Since the Reynolds number in a microfluidic device is very low ($Re < 100$), distinct lamellae are formed, with minimal advection of species occurring between them. Therefore, biological materials can be effectively trapped within their own stream with secondary sheath flows on one or more sides. Using the consistent magnetostatic forces generated by two NdFeB magnets (see Chapter 4 for details), paramagnetic particles can then be transported out of the primary flow without affecting the other constituents (Figure 1). To maximize the surface area for micromagnetic separation while maintaining a two-dimensional profile, two dual sheath flow setups were proposed, where the primary flow of blood interacts with two sheath flows. The first setup was manufactured using SU-8 photolithography and PDMS (polydimethylsiloxane) soft lithography, and finally tested using saline flow.

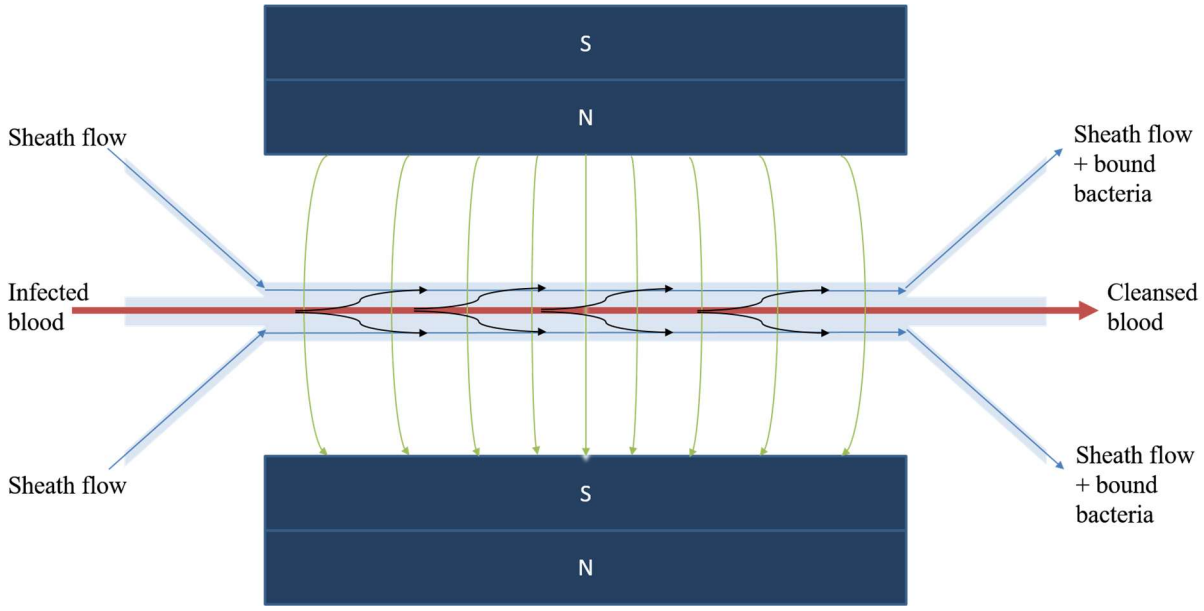

Figure 1: Schematic of magnetic separation principles. Infected blood enters the central inlet on the left (red) and sheath fluid enters the other inlets (blue). Paramagnetic particles and bound bacteria are separated by the magnetic force into the sheath flows (black).

2.2. Materials and methods

2.2.1. Microfluidic design

The microfluidic design was developed using a three-input, three-output framework and drafted in Autodesk AutoCAD 2016. Incubated blood enters from a central channel and interacts with two sheath flows on either side. These devices focused the three flows into a single main channel 300 µm in width and 25 mm in length; the central channel width was varied between 50, 100, 150, and 200 µm, while each of the sheath flows had a width of half the remainder (i.e., 125, 100, 75, and 50 µm, respectively). The sheath flows entered the main channel at ± 45° (Figure 2).

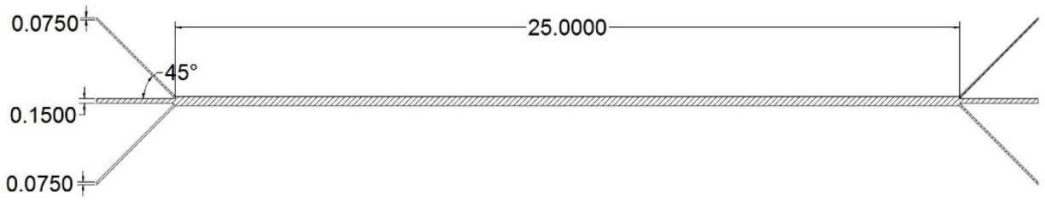

Figure 2: Schematic of microfluidic device, with 0.150mm width for the central channel. Units in millimeters. Hatched space indicates where fluid flows.

2.2.2. SU-8 photolithography

Masters for the microfluidic devices were fabricated with SU-8 photolithography [39]. First, a 4" (1 1 1) monocrystalline silicon wafer was cleaned with acetone and isopropanol while spinning at 3000 rpm. The wafer rotation was then stopped and SU-8 2050 photoresist was poured onto it. To produce a 50 µm-thick layer, the wafer was spun at 500 rpm for 15 s and then accelerated to 2500 rpm for 35 s. During the last 10 s of spinning, any edge bead was removed with acetone. The wafer was subsequently baked at 95°C for ten minutes, covered by a crystallization dish with an air gap. After baking, a Mylar mask was aligned on the surface of the photoresist. The photoresist was exposed to a UV dose of 220 J/cm^2; this was achieved by measuring the UV lamp's intensity and calculating the necessary time. The wafer was then baked again at 95°C for ten minutes. SU-8 developer was then poured onto the wafer, spun under a stream of isopropanol, and dried with nitrogen. For the final hard bake, the wafer was placed onto a hotplate with a 60°C/h ramp and a maximum temperature of 150°C, baked at the maximum temperature for five minutes, and then cooled on the hotplate. The feature height was measured using a contact profilometer.

2.2.3. PDMS soft lithography and plasma bonding

Once a master was made, devices could be fabricated using PDMS soft lithography [39]. Briefly, PDMS and a cross-linking agent were mixed in a 10:1 ratio and poured onto the SU-8 master in a 6" plastic dish. This was then put in a vacuum desiccator for one minute to remove dissolved gasses; resultant bubbles were removed using light application of an air gun. The PDMS was then cured at 65°C for three hours. After curing, the area around the devices was cut out and divided into individual devices. For assembling a single device, a 25 mm x 75 mm x 1 mm microscope slide was cleaned with isopropanol and holes were punched into the inlets and outlets of the PDMS using a 1.5mm biopsy punch. The sides of the slide and PDMS to be bonded were placed face up into a plasma chamber and exposed for 50 s. Promptly after removal, the slide and PDMS were pressed firmly together.

2.2.4. Volumetric flow testing

To characterize the flow patterns of the devices, a simple volumetric flow test was devised. Tygon tubing (1/16" outer diameter) was used to connect a device to two 10 mL Luer-Lok syringes. To provide flow to both of the sheath flows, a 25-gauge needle Y-connector (Instech Laboratories, Inc.) was used in between the sheath flow syringe and the inlets on the device. The device outlets fed into microfuge tubes for collection. Two milliliters of phosphate-buffered saline (PBS) from each syringe (total of 4mL) was flowed through the device at either 0.2 mL/min, 0.5 mL/min, or 1.0 mL/min using a syringe pump. The volume of PBS in each of the outlet collection tubes was record after flow was completed. Ratios of the central channel flow output to the sheath outputs' combined flow were statistically compared across the varying central channel widths and flow rates by two-way ANOVA.

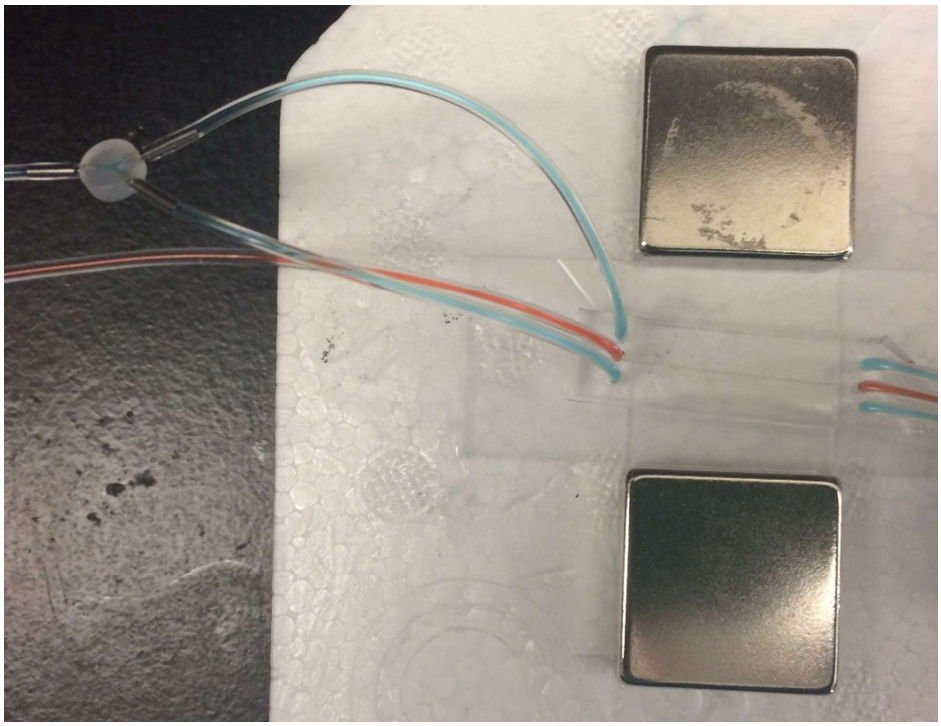

Figure 3: Assembled microfluidic device. On the left are the inlets with the Y-connector for the sheath flows. The device with two NdFeB magnets is shown on the right. Here, the central flow is shown in red and the sheath flows are dyed blue.

2.3. Results and discussion

The four variations of the microfluidic device were placed in triplicate onto a Mylar mask to expedite fabrication (Figure 4). Additional marks were made to the side of the main channel to allow for reducing the magnetic separation distance. However, these were not used because the PDMS was too thin to resist tearing before plasma treatment. The master resulting from SU-8 photolithography had a feature height of 68.8 ± 7.4 μm, which was deemed sufficient for initial testing (Figure 5); future devices may need more stringent control. PDMS devices were very stable, capable of remaining intact with flow rates >2 mL/min, presumably due to their short channel length and relatively large channel width. To interpret volumetric flow results, the

normalized ratio of volume from the central channel outlet compared to the sum of the sheath flows was used; the ideal ratio for all devices was 1, since 2 mL of fluid was flowing through the central and sheath channels, respectively. However, none of the devices were able to maintain this ratio. All but the 50 µm devices had an average ratio greater than 1, indicating that a substantial amount of fluid was exiting out of the center instead of remaining in the sheath flow, regardless of flow rate ($p > 0.05$). *Post hoc* analysis across the central channel widths shows some significance between certain devices, but not amongst all of them (Figure 6). If these devices were to be implemented in *in situ*, this would imply that sheath fluid would be entering the patient. As such, these devices were determined to be poor candidates for micromagnetic separation.

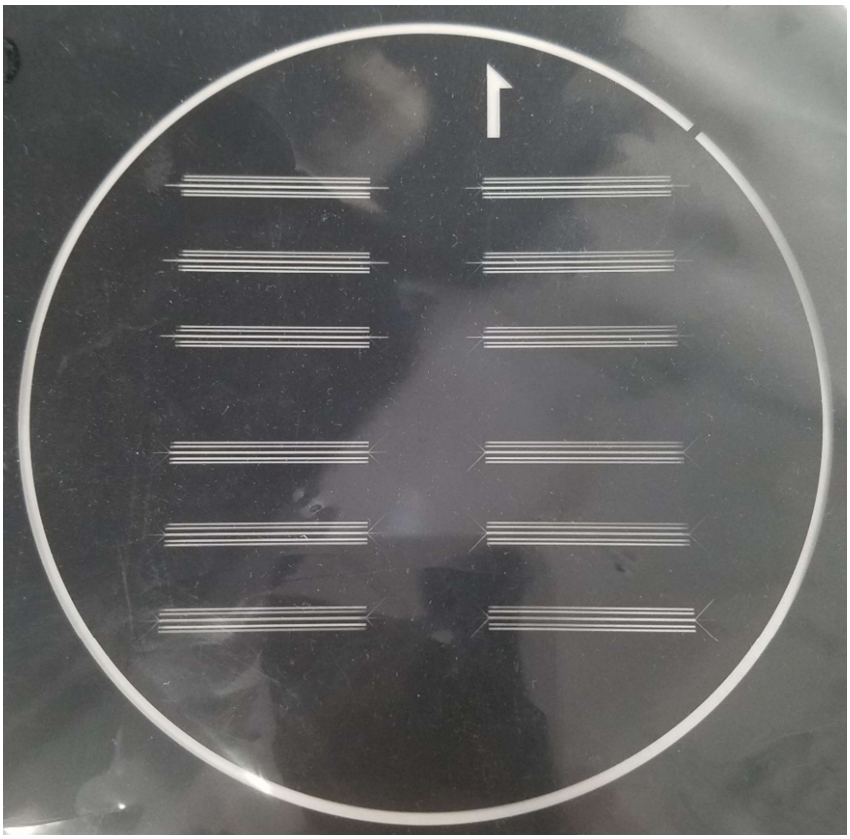

Figure 4: Mylar mask for fabrication of microfluidic devices. The central channel has a width of, from the top right going clockwise, 150 µm, 50 µm, 100 µm, and 200 µm.

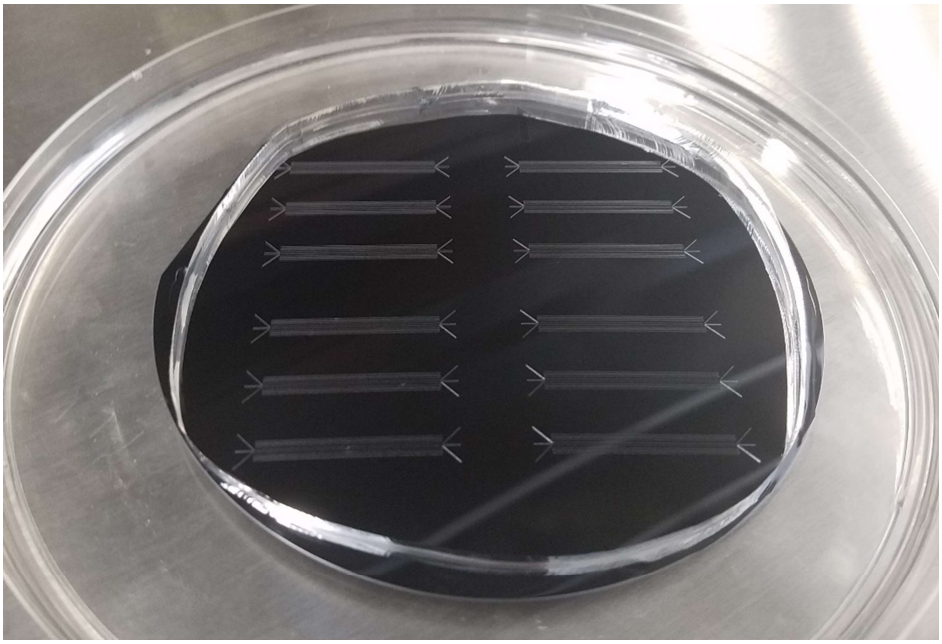

Figure 5: SU-8 master in PDMS

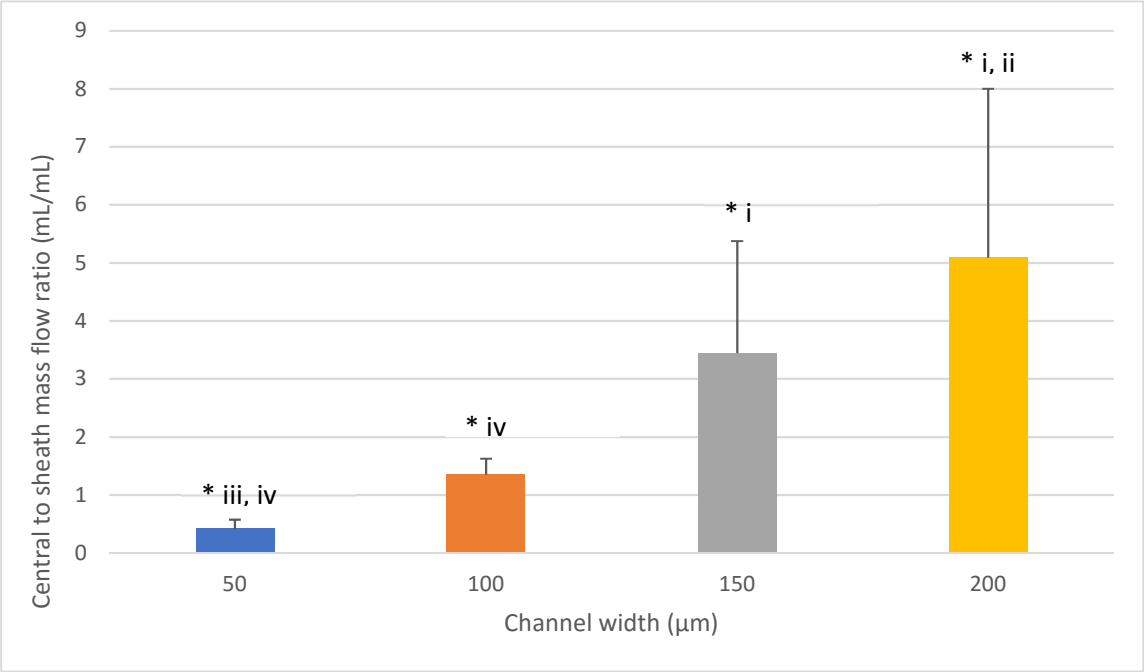

Figure 6: Results of volumetric flow test for microfluidic devices. Mean ± standard deviation. The 100 µm devices had a ratio close to 1, while the 50 µm devices had a ratio less than 1 and the others had a ratio greater than 1. More fluid was coming out of the central channel in the case of the 150 µm and 200 µm devices. Roman numerals indicate statistical significance to other devices (numbered left to right).

2.4. Conclusion

SU-8 photolithography and PDMS soft lithography are the methods of choice for microfluidic fabrication, since they are relatively easy and can produce several microfluidic devices from a single master. In this chapter, the successful production of microfluidic devices intended for micromagnetic separation was demonstrated. However, these devices did not properly isolate the sheath flows from the central flow, leading to mixing of fluids upon exit. This mixing is less than ideal for a clinical setting, since additional, potentially contaminated fluid would return to the patient. More investigation into maintaining sheath flow in a microfluidic device needed to be done before any further testing could occur.

CHAPTER 3

Computational fluid dynamics of sheath flow in microfluidic devices

3.1. Introduction

Informed design of microfluidics necessitates some exploration into fluid mechanics. The velocity, pressure, and other field variables have a great impact on the application of a microfluidic device. To solve the governing partial differential equations for fluid flow, numerical methods must be used, the preferred of which are finite element methods (FEM). The first and second generation microfluidic devices were analyzed for maintenance of a sheath flow informed by velocity profiles and mass fluxes.

3.2. Materials and methods

ANSYS' Fluent 17.2 was used for all computational fluid dynamics simulations. A two-dimensional, steady-state analysis was employed since it is more stable than three-dimensional problems and information in the z-direction or over time is not as important given the aspect ratios seen in microfluidics. Symmetry conditions were used where possible to reduce computational burden.

Fluent solves the incompressible two-dimensional Navier-Stokes equation for flow

$$\rho \frac{\partial}{\partial t}\mathbf{v} + \rho \nabla \cdot (\mathbf{v}\,\mathbf{v}^{\mathrm{T}}) = -\nabla P + \mu \nabla \cdot (\nabla \mathbf{v} + \nabla \mathbf{v}^{\mathrm{T}}) \tag{1}$$

in conjunction with the conversation equation,

$$\nabla \cdot \mathbf{v} = 0 \tag{2}$$

, where ρ is the fluid density, $\mathbf{v}$ is the fluid velocity, P is the pressure, and μ is the fluid's dynamic viscosity. These equations are solved simultaneously using the SIMPLE pressure-based

algorithm, a least squares cell based gradient, a second order pressure scheme, and a second order upwind momentum scheme. Since the maximum Reynolds number is much less than the critical Reynolds number of 2000 (Re_{max} = 400), a laminar model was used. A Newtonian model of saline with a constant density of 1.06 g/cm^3 and a constant dynamic viscosity of 1.003 x 10^{-3} Pa·s was chosen for the fluid. No-slip boundary conditions were implemented for the walls, while a zero gauge pressure was specified at the outlets. The inlets for each of the channels were specified with a mass flow rate of 0.0042 g/s based on symmetry conditions. Each device was meshed using the uniform setting with maximum face size of 25 μm, 10 μm, 7.5 μm, or 5 μm to determine mesh independence of the solutions – that is, that the solution does not depend on the mesh – via mass flow rates at the outlets. The solver was run until a relative error of 10^{-8} between iterations was reached.

Second-generation devices employed a curved design and divided the separation regions into two distinct channels. This iteration on the previous generation improves the magnetic flux density gradient present in the separation channels, while also ensuring consistent fluidic resistance at the flow outlets. All of the inlets and outlets had the same width of 200 μm (Figure 7). This geometry was analyzed in the same manner as their first-generation counterparts.

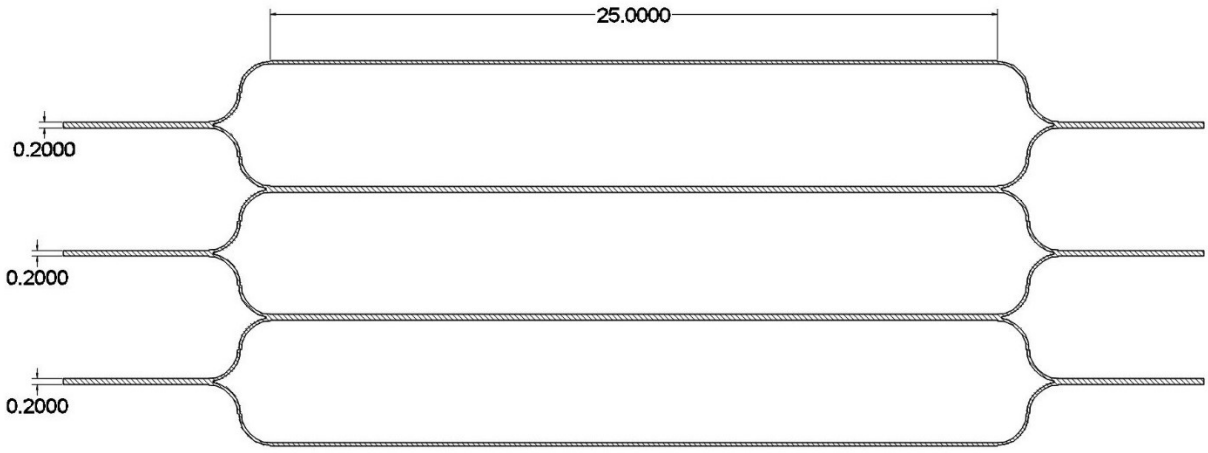

Figure 7: Schematic of second-generation device. Units in millimeters. Hatched space indicates where fluid flows.

3.3. Results and discussion

Mesh independence was readily achieved for the 100 μm and 150 μm first-generation devices; relative errors were within 3% between the 7.5 μm and 5.0 μm meshes (Figure 8). Convergence was more difficult to establish for the 50 μm and 200 μm first-generation devices and the second-generation devices because their geometries could not be discretized well by a coarse mesh; however, the residuals did decrease to less than 10^{-3}, which is acceptable in some scenarios [40]. The ratio of main channel flow to sheath flow shows a trend that agrees with the experimental results. However, the magnitudes of the simulated ratios are much greater for devices larger than 100 μm and smaller for the 50 μm device (Table 1). This large discrepancy may be due to surface tension and three-dimensional effects that are not captured in this two-dimensional model. Nevertheless, the second-generation device shows some promise, since the main-to-sheath flow ratio was approximately 1.31. The velocity profiles of the devices agree with the differences in mass flow, with devices with main channel widths larger than 100 μm

demonstrating predicted hydrodynamic focusing towards the main outlet, while the 50 µm device shows a marked decrease in velocity for the main outlet (Figure 9 - Figure 12). The second-generation device shows some improvement over the first-generation designs. The mass flow ratio is simulated to be 1.31, which is closer to 1 than any of the first-generation devices. Furthermore, the velocities for the sheath outlets are much closer to the velocities at the blood outlet when compared to the first-generation devices (Figure 13).

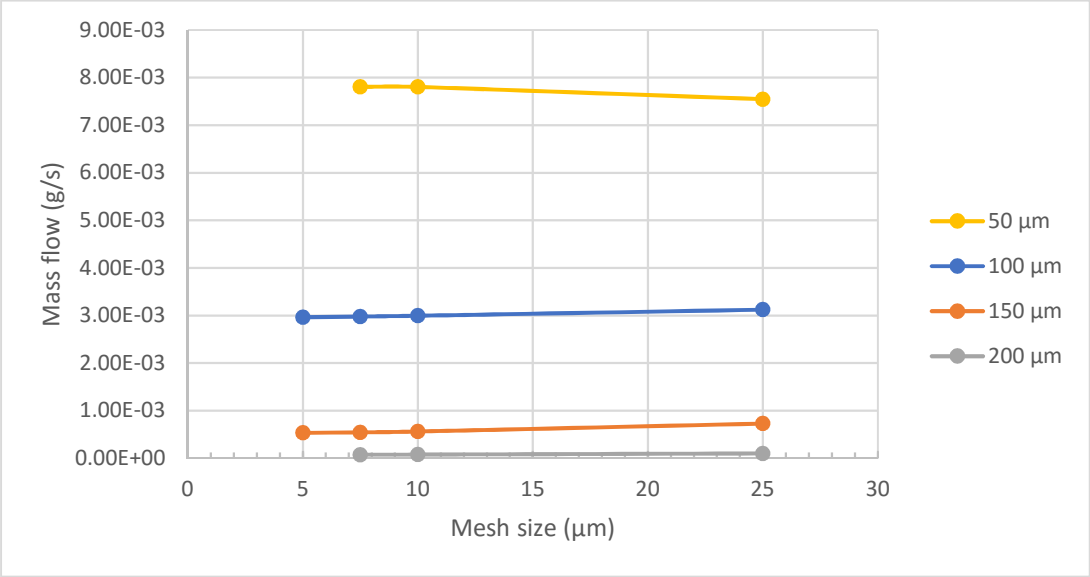

Figure 8: Mesh independence study for first-generation devices based on mass flow rate through left sheath outlet. 5 µm mesh size omitted from 50 µm and 200 µm devices due to failure to generate mesh. Less than 3% variation is seen between the finest meshes for the 100 µm and 150 µm devices.

Table 1: Experimental versus simulated mass flow ratios for first-generation devices.

Central channel width (μm)	Experimental mass flow ratio	Simulated mass flow ratio
50	0.42	0.13
100	1.35	1.98
150	3.45	15.55
200	5.09	116.08

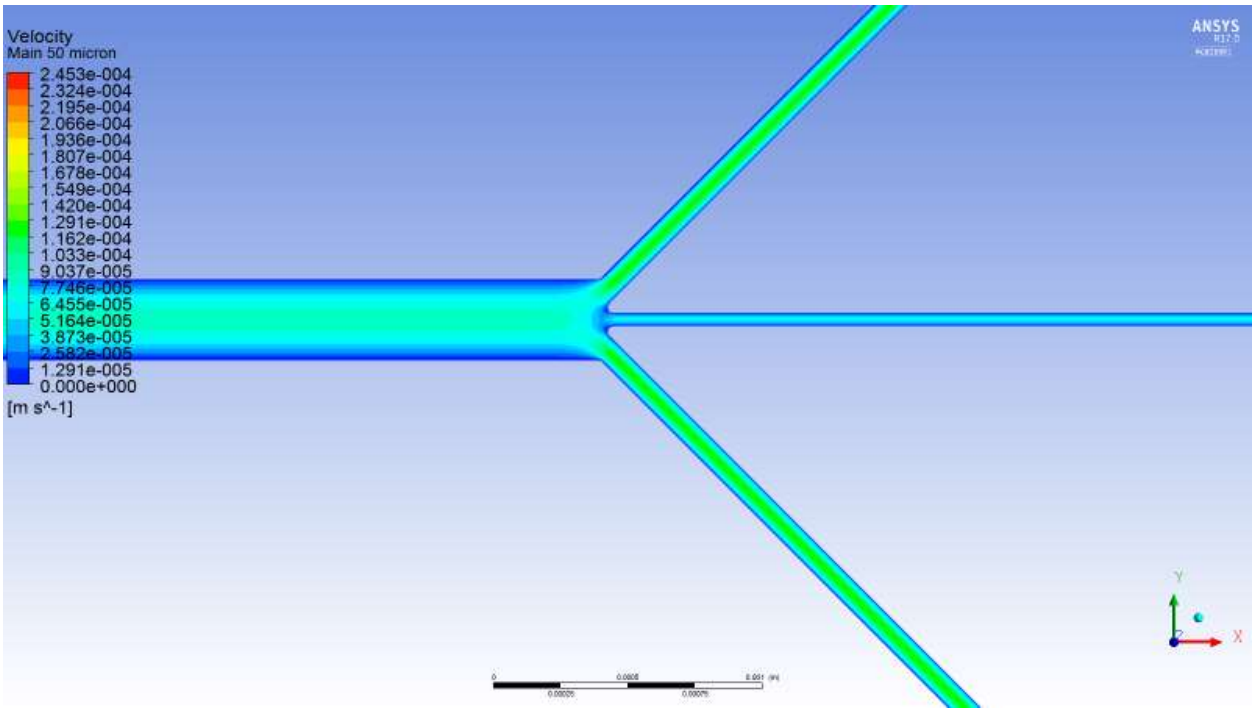

Figure 9: Velocity profile at outlet for 50 μm device.

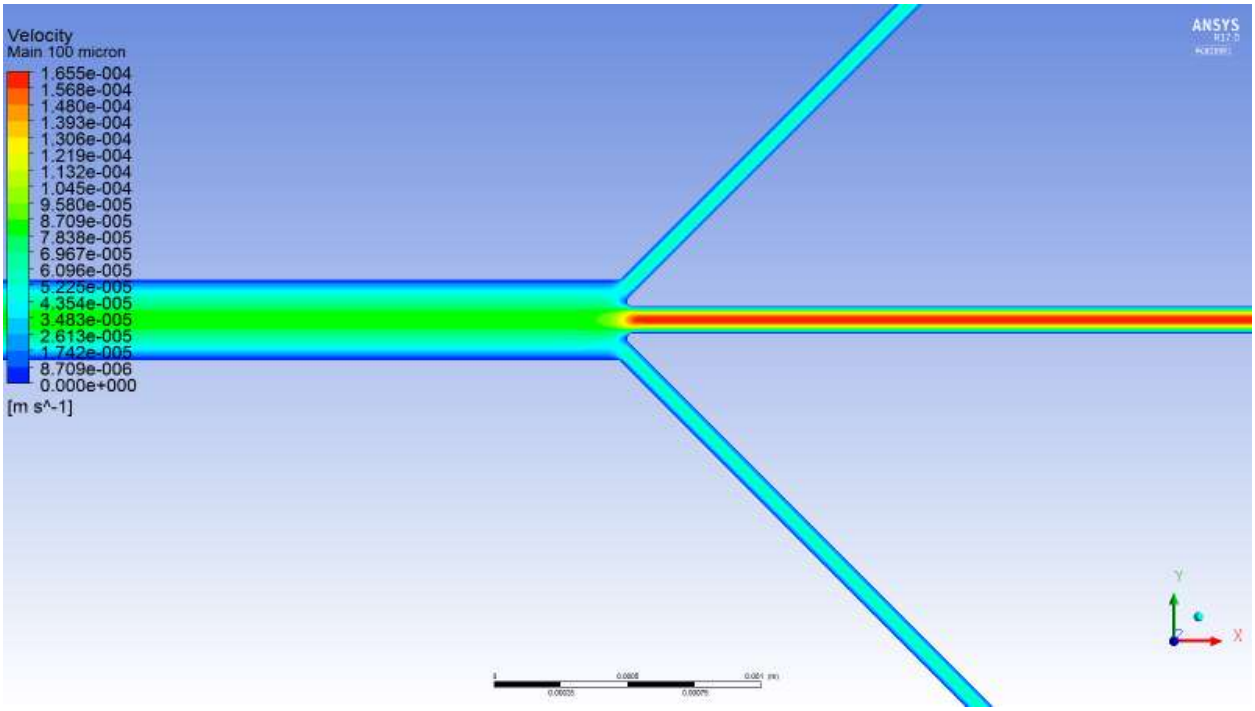

Figure 10: Velocity profile at outlet for 100 µm device.

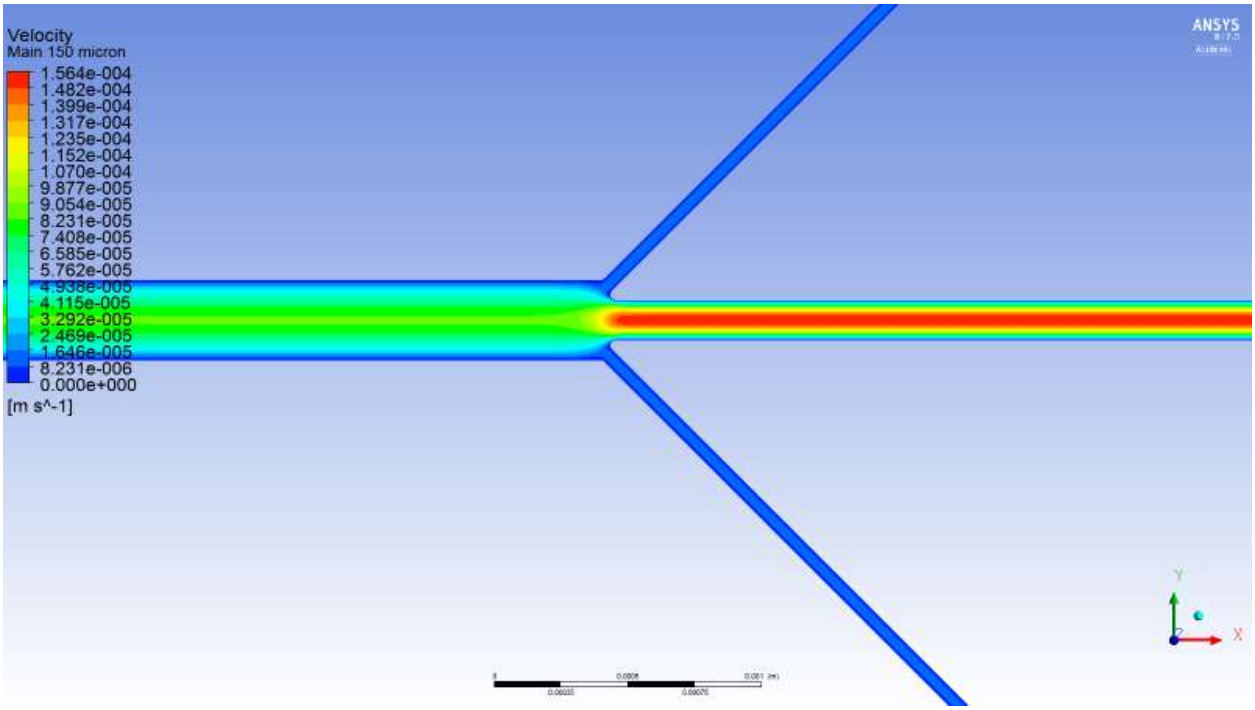

Figure 11: Velocity profile at outlet for 150 µm device.

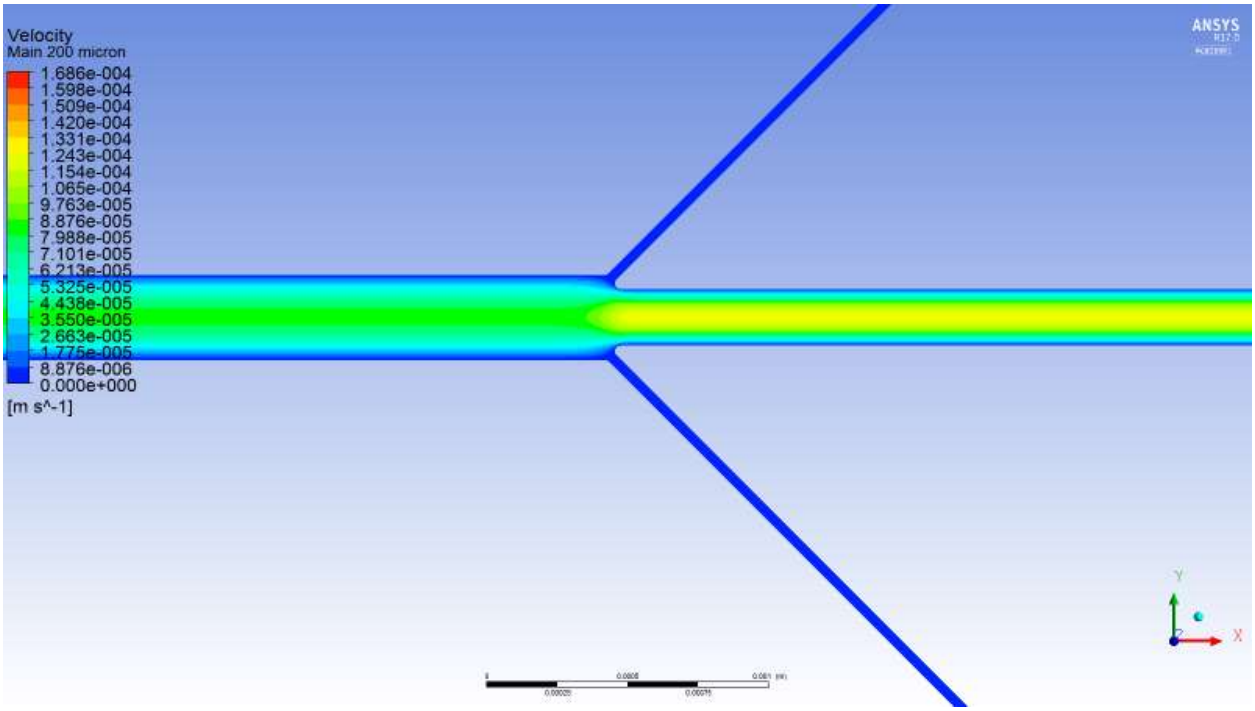

Figure 12: Velocity profile at outlet for 200 µm device.

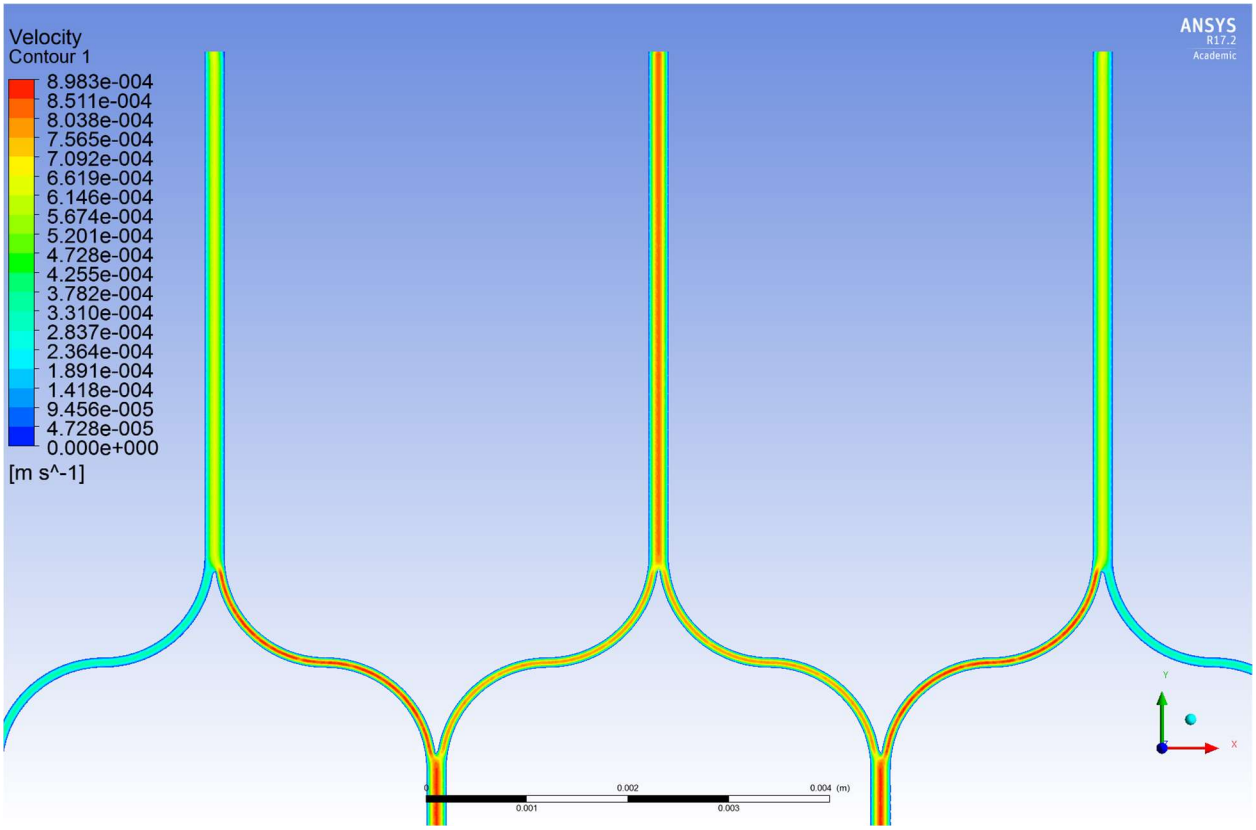

Figure 13: Velocity profile at outlet for second-generation device.

3.4. Conclusion

Computational fluid dynamics is a powerful analysis tool for microfluidics. It can make visible properties that are not readily apparent by other techniques and can inform design and redesign. The first-generation devices previously described are ill-suited for magnetic separation because they have a tendency to focus flow to the largest outlet rather than maintaining distinct lamellae. Additional investigation into this modeling could be carried out. For example, three-dimensional effects can be incorporated into fluidics models, also this tends to be more computationally expensive. Additionally, various models for blood on this length scale exist and should be taken into consideration when designing blood-centric microfluidic devices.

CHAPTER 4

Magnetostatic modeling of separation device

Text adapted from:

Petty Valenzuela, Stephen N., Sinead E. Miller, Charleson S. Bell, Todd D. Giorgio. "Optimization of micromagnetic separation for bacteremia treatment." *2nd International Conference on Nanomedicine, Drug Delivery, and Tissue Engineering*, Barcelona, Spain, 2017.

4.1. Introduction

To calculate the motion and thus the separation of paramagnetic particles, the magnetic field used must be quantitatively described. Specifically, the force on paramagnetic particles is directly proportional to the magnetic flux density gradient, represented here as $|\nabla B^2|$. The partial differential equations (PDEs) that describe the magnetic field and magnetic flux density cannot be solved analytically if complex geometries are involved, such as the field produced by multiple magnets. In this chapter, the magnetic field to be used in the separation device is explored in various magnet configurations to optimize the separation of paramagnetic particles.

4.2. Materials and Methods

The program FEMM 4.2 was used to calculate the magnetic field, **H**, and flux density, **B**, of the magnets. The general time-invariant magnetostatic problem has the governing equations

$$\nabla \times \mathbf{H} = \mathbf{J} \tag{3}$$

$$\nabla \cdot \mathbf{B} = 0 \tag{4}$$

where **J** is the current density. The constitutive equation relating the field to the flux density by the permeability, μ,

$$\mathbf{B} = \mu\mathbf{H} \tag{5}$$

must be used for each linear material in the domain. FEMM solves these equations using a magnetic vector potential approach, defining the magnetic flux density in terms of a vector potential, **A**,

$$\mathbf{B} = \nabla\times\mathbf{A} \tag{6}$$

This allows the magnetic field governing equation to be rewritten as

$$\nabla\times\left(\frac{1}{\mu}\nabla\times\mathbf{A}\right) = \mathbf{J} \tag{7}$$

and **A** can be solved for using finite element analysis (FEA). **B** and **H** can then be derived from **A**.

Two rectangular neodymium (NdFeB) magnets (K&J Magnetics, BX04X0, Grade N42 NdFeB, 1" x 1/4" x 1" thick, $\mu_r = 1.05,\ H_c = \ 1006582\ \mathrm{A/m}$) were simulated via FEA in an attracting configuration with a separation distance of 25mm, equivalent to the width of the device. The poles of these magnets are located on the 1/4" thick sides rather than on the square faces, making them ideal for a low-profile separator. The flux density field across the gap in the y-direction was obtained and then differentiated in Matlab 2015a to determine the magnetic flux density gradient, represented here as $|\nabla B^2|$.

4.3. Results and discussion

The domain near two rectangular NdFeB magnets was simulated with 4574 nodes and 8721 elements via FEA. The calculated two-dimensional magnetic flux density is comparable to the manufacturer's documentation [41] (Figure 14). A parabolic profile with a maximum flux

density of 0.521T and a minimum field strength of 0.360T across the channel was estimated (Figure 15). The magnetic flux density gradient ranges from approximately -20 T^2/m to 20 T^2/m; discretization error from differentiation resulted in a non-smooth curve (Figure 16). At the location of the microfluidic channels, 2.1mm from the center of the space between the magnets, the magnetic flux density gradient was calculated to be 4.7 T^2/m. With this magnetic flux field, a linear magnetic flux density gradient can be established to ensure consistent separation of magnetic complexes.

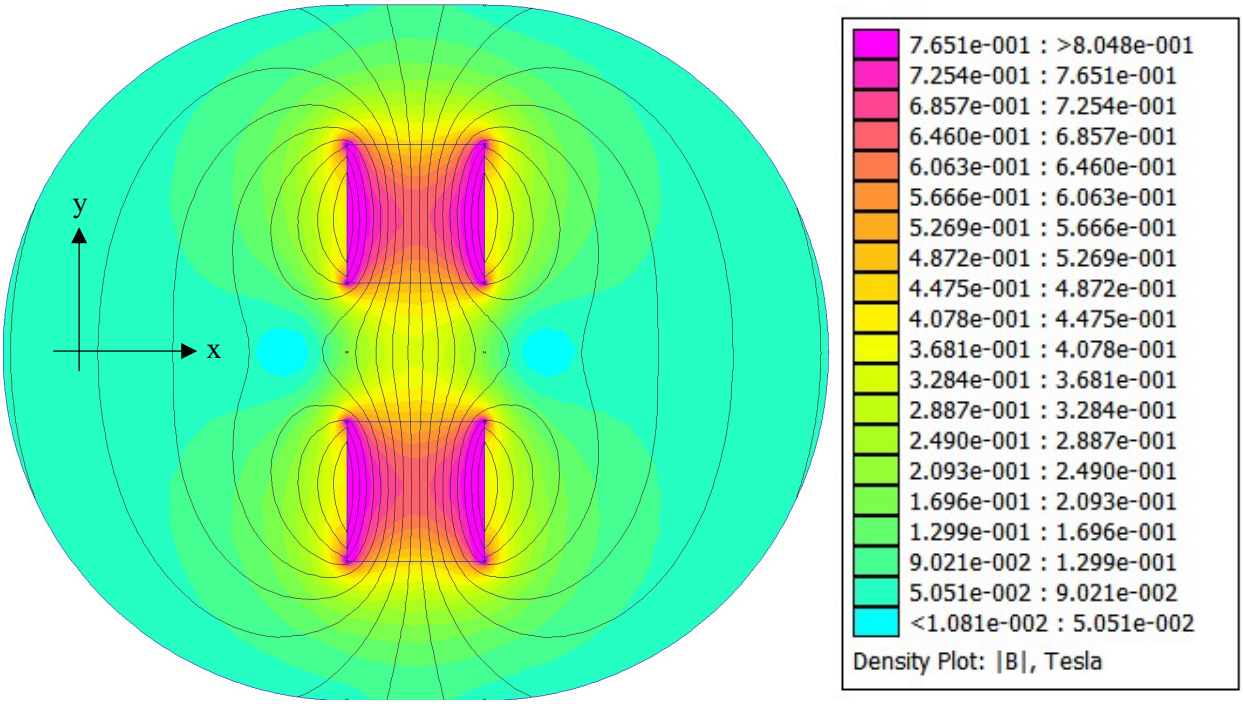

Figure 14: Magnetic flux density plotted over domain. Fluid flow is in the x-direction.

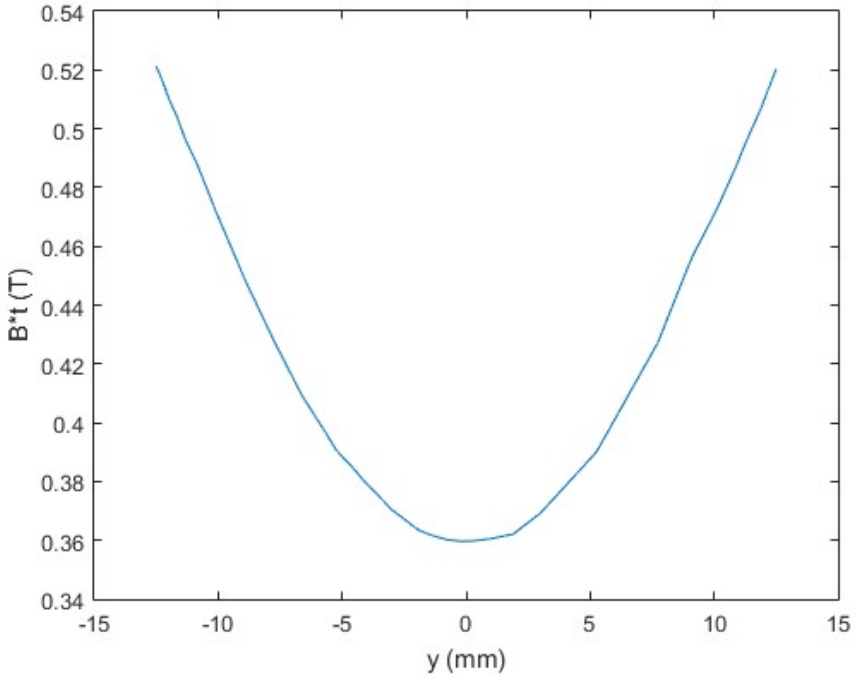

Figure 15: Magnetic flux density in vertical direction.

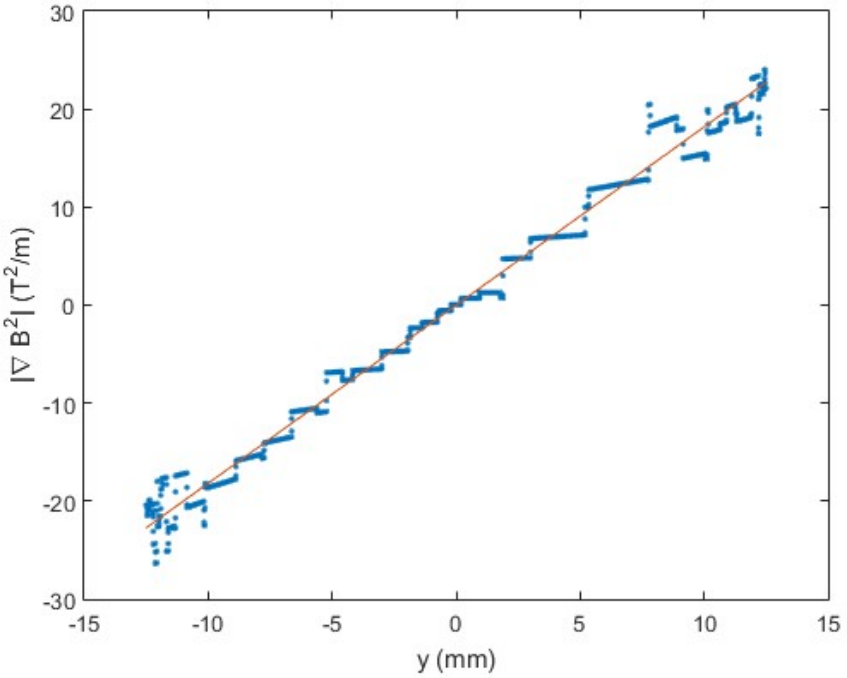

Figure 16: Magnetic flux density gradient in vertical direction. Regression line (red): $|\nabla B^2| = 1.8182 \frac{\mathrm{T}^2}{\mathrm{m}} \frac{y}{\mathrm{mm}}$, $R^2 = 0.9872$.

4.4. Conclusion

Magnetostatic modeling of the two-magnet configuration produces a parabolic magnetic flux profile and a linear magnetic flux density gradient. At the point halfway between the two magnets, the magnetic flux density gradient is at or near zero, meaning microfluidic channels for separation must be offset from the center to achieve efficient separation. A further advantage to this linear profile is that magnetic particles should be drawn outward, regardless of which side of the device the particle is on.

CHAPTER 5

Physiologically-based pharmacokinetic model with physically-based separation model

Text adapted from:

Petty Valenzuela, Stephen N., Sinead E. Miller, Charleson S. Bell, Todd D. Giorgio. "Optimization of micromagnetic separation for bacteremia treatment." *2nd International Conference on Nanomedicine, Drug Delivery, and Tissue Engineering*, Barcelona, Spain, 2017.

5.1. Introduction

The removal of bacteria from the various infected organs can be modeled as a clearance mechanism, lending credence to a multi-compartmental physiologically-based pharmacokinetic (PBPK) model. PBPK models of bacterial infection have been in existence since at least Cheewatrakoolpong et al.'s two-compartmental murine model [42]. Miller et al. were the first to incorporate an extracorporeal pathogen removal device into an infection model [16]. A magnetic separation model was developed by Kang et al. for their device, interrogating the role of the radius of their magnetic beads in separation efficiency from whole blood [38]. Combining these models allows for better understanding of the pharmacokinetics of extracorporeal pathogen removal via magnetic beads and can inform the selection of bead radius, incubation times, and device flow rates.

5.2. Materials and Methods

5.2.1. Analytic model of magnetic separation

The binding efficiency of particles to *A. baumannii* was estimated. As discussed by Kang et al., the concentration of bound bacteria, c_0, as a function of microsphere radius and incubation time can be expressed as

$$c_0(r_b, t_{inc}) = c_0^{in} \exp(-c_e(k_d + k_{shear})bt_{inc}) \tag{8}$$

where c_0^{in} is the initial concentration of bacteria; c_e is an empirical constant to account for changes in binding efficiency in biologically relevant fluids; k_d and k_{shear} are the collision rate constants of diffusion and shear, given respectively by

$$k_d = \frac{2r_c k_B T}{3\eta r_b} \tag{9}$$

$$k_{she} \quad = \pi\dot{\gamma}(r_b + r_c)^3 \tag{10}$$

with Boltzmann's constant, k_B, the ambient temperature, T, the viscosity of blood, η, the spherical radius of the cell, r_c, and the empirically determined shear rate, $\dot{\gamma}$, held constant; b as the concentration of microspheres calculated relative to a given concentration of r_b = 500 nm microspheres by

$$b = b_{500\text{ nm}}\left(\frac{500\text{ nm}}{r_b}\right)^3 \tag{11}$$

and t_{inc} as the incubation time. The overall binding efficiency, x, is therefore estimated as

$$x(r_b, t_{inc}) = 1 - \frac{c_0(r_b, t_{inc})}{c_0^{in}} = 1 - \exp(-c_e(k_d + k_{shear})bt_{inc}) \tag{12}$$

After incubation, the microspheres and microsphere-bacteria complexes are separated out via the magnetophoretic force,

$$F_{mag} = N\frac{4\pi r_b^3}{3}\frac{\chi_v}{2\mu_0}|\nabla B^2| \tag{13}$$

with the constants μ_0, the vacuum magnetic permeability; χ_v, the volumetric susceptibility of the microspheres; and $|\nabla B^2|$, the magnetic flux density gradient. N is the number of microspheres bound to a bacterium and is estimated by

$$N(r_b) = 4\rho\left(\frac{r_c}{r_b}\right)^2 \tag{14}$$

Here, ρ refers to the estimated proportion of the cell surface covered by microspheres.

Opposing the magnetophoretic force is the drag force in terms of the magnetophoretic velocity, v_{mag}, given by Stokes flow

$$F_{drag} = 6\pi r_n \eta v_{mag} \tag{15}$$

where r_n is the effective hydraulic radius of a microsphere-bacterium complex given by

$$r_n = \sqrt[3]{r_c^3 + N r_b^3} \tag{16}$$

Solving $F_{mag} = F_{drag}$ for v_{mag} under the assumption of force equilibrium, the magnetophoretic velocity of the complexes is equal to

$$v_{mag} = \frac{N r_b^3 \chi_v |\nabla B^2|}{9\eta\mu_0 r_n} \tag{17}$$

Therefore, the magnetic separation time across the width of the channel, w, can be calculated as

$$t_{mag} = w/v_{mag} \tag{18}$$

Assuming steady flow in the separation channels, the average velocity of a complex is given by

$$\overline{v_f} = \frac{Q_E}{nA} \tag{19}$$

Q_E being the volumetric flow rate through the entire device, n being the number of channels, and $A = hw$ being the rectangular cross-sectional area of a channel with height h and width w. The residence time in the channel with length l can be calculated as

$$t_{res} = l/\overline{v_f} \tag{20}$$

The magnetic separation efficiency m is then estimated by

$$m(r_b, Q_E) = \begin{cases} \frac{t_{res}}{t_{mag}} & , t_{res} < t_{mag} \\ 1 & , t_{res} \geq t_{mag} \end{cases} \tag{21a}$$

$$= \begin{cases} \frac{4nhl\rho r_b r_c^2 \chi_v |\nabla B^2|}{9Q_E \eta \mu_0 (r_c^3 + 4\rho r_b r_c^2)^{1/3}} & , t_{res} < t_{mag} \\ 1 & , t_{res} \geq t_{mag} \end{cases} \tag{19b}$$

After the incubation and separation stages, the overall fraction of bacteria removed can be expressed as

$$f(r_b, Q_E, t_{inc}) = x(r_b, t_{inc}) * m(r_b, Q_E) \tag{22}$$

Table 2 lists the physical constants and parameters used for all of the simulations. The device-specific parameters (width, height, length, and number of channels) are based on the second-generation microfluidic design detailed in Chapter 2.

Table 2: Constants for magnetic separation efficiency calculations. Magnetic flux density gradient is as determined in magnetostatic FEA.

Parameter	**Value and units**	**Parameter**	**Value and units**
c_0^{in}	10^7 CFU/mL	χ_v	3.5
c_e	3.7 x 10^{-4}	ρ	0.5
T	300 K	w	1 x 10^{-4} m
η	4.0 x 10^{-3} kg m^{-1} s^{-1}	n	2
r_c	0.5 x 10^{-6} m	h	5 x 10^{-5} m
$\dot{\gamma}$	1.0186 s^{-1}	l	2.5 x 10^{-2} m
$b_{500\,\mathrm{nm}}$	0.0025 kg m^{-3}	$\lvert\nabla B^2\rvert$	4.7 T^2/m

5.2.2. Multi-compartment physiologically-based pharmacokinetic infection model

The fractional magnetic separation from Equation 22 factors into the five-compartment PBPK model of infection diagrammed in Fig. 1 and detailed in Equations 23-27. Each physiologic compartment has its own associated growth rate, G_i, a blood volume, V_i, blood flow rate, Q_i, and a partition coefficient to bacteria, p_i (Table 3). The transport of bacteria between compartments is represented by the arrows in Figure 17. The most significant modification from the model published by Miller et al.[16] is the removal of the return pathway from the device to the blood; here, the assumption is that any bacteria removed by the device has no path of reentry into the circulatory system.

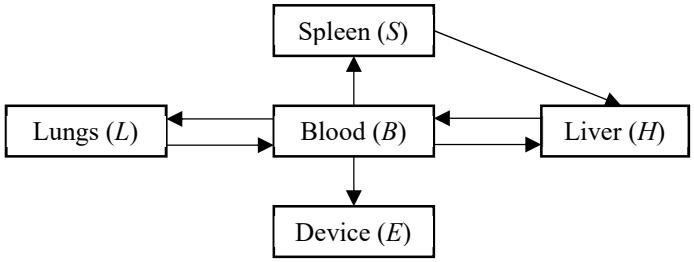

Figure 17: Diagram of infection compartmental model. Arrows indicate blood flow between the compartments. Letters in parentheses indicate symbols used for the compartmental concentrations in the equations.

$$\frac{dL}{dt} = G_L L + \frac{Q_L}{V_L} B - \frac{Q_L}{\mathrm{p}_L V_L} L \tag{23}$$

$$\frac{dS}{dt} = G_S S + \frac{Q_S}{V_S} B - \frac{Q_S}{\mathrm{p}_S V_S} S \tag{24}$$

$$\frac{dH}{dt} = G_H H + \frac{Q_H}{V_H} B + \frac{Q_S}{\mathrm{p}_S V_S} S - \frac{Q_H + Q_S}{\mathrm{p}_H V_H} H \tag{25}$$

$$\frac{dB}{dt} = G_B B + \frac{Q_H + Q_S}{\mathrm{p}_H V_H} H + \frac{Q_L}{\mathrm{p}_L V_L} L - \left(\frac{Q_L}{V_L} + \frac{Q_S}{V_S} + \frac{Q_H}{V_H} + f(r_b, Q_E, t_{inc}) \frac{Q_E}{V_E} \right) B \tag{26}$$

$$\frac{dE}{dt} = f(r_b, Q_E, t_{inc}) \frac{Q_E}{V_E} B \tag{27}$$

Six different infection and treatment scenarios were then simulated using the coupled models: a non-immunocompromised human, an immunocompromised human, an immunocompromised human with antibiotic administration, and using the extracorporeal device with the three previous scenarios. A simulated bolus of 10^7 CFU/mL of *A. baumannii* was injected into the lung compartment and allowed to proliferate in the system for ten hours. After incubating the blood with the colistinated magnetic microspheres for $t_{inc} = 5$ min, the extracorporeal device was linked into the system and ran for 96 hours. To determine the efficacy of treatment, the area under the curve (AUC) via trapezoidal integration in each of the compartments was compared across flow rates and microsphere radii. As a quantifiable criterion, the time to go below a threshold of 1 CFU/mL in the bloodstream was also examined [16].

Matlab 2015a's 4th-order Runge-Kutta solver was used to calculate an approximate solution to the system of differential equations (Appendix).

Table 3: Parameters for PBPK model of *A. baumannii* infection.

IC = immunocompromised AB = antibiotic + immunocompromised			$\mathbf{p_i}$		$\boldsymbol{G_i}$ **(h^{-1})**		
Compartment	$\boldsymbol{Q_i}$ **(m^3 h^{-1})**	$\boldsymbol{V_i}$ **(m^3 h^{-1})**	**Normal**	**IC**	**Normal**	**IC**	**AB**
Lungs	0.08995	4.50×10^{-4}	93	3	-1.74	0.21	-0.24
Spleen	0.01501	2.09×10^{-4}	59	28	-0.14	0.14	-0.07
Liver	0.0483	1.56×10^{-3}	749	79	-0.10	0.10	-0.18
Blood	N/A	N/A	N/A	N/A	-0.17	0.08	-0.05
Device	variable	2.5×10^{-10}	1	1	N/A	N/A	N/A

5.3. Results and discussion

Using the magnetic flux density gradient from the previous magnetostatic simulation, the magnetic separation of microsphere-bacteria complexes was modeled for microspheres with radii from 25nm to 500nm, which correspond to common paramagnetic microspheres. The device flow rate was varied over the typical range of microfluidic flow rates, 0.01mL/min to 1.5mL/min. Infection metrics, including maximum bacterial load, time to threshold, and area under the curve, did not change significantly with microsphere radius or flow rate. The standard deviation of any metric is at least two orders of magnitude smaller than the mean (Table 4). Bacterial loads do not change significantly with the incorporation of the extracorporeal device, despite quantifiable bacterial capture in comparison with the absence of extracorporeal bacterial separation (Figure 18).

Table 4: Infection metric statistics across parameter space. Mean ± standard deviation. N/A here indicates that the compartment's bacterial load never went below 1 CFU/mL.

	Compartment	Max. load (CFU/mL)	Time to threshold (h)	AUC (CFU/mL * h)
Non-immunocompromised	Lungs	$1.32 \times 10^{4} \pm 6.82 \times 10^{-10}$	75.97 ± 0.001	$1.06 \times 10^{5} \pm 8.09 \times 10^{0}$
	Spleen	$1.45 \times 10^{4} \pm 4.02 \times 10^{-10}$	76.72 ± 0.002	$1.16 \times 10^{5} \pm 8.33 \times 10^{0}$
	Liver	$8.66 \times 10^{5} \pm 5.47 \times 10^{-9}$	N/A	$6.93 \times 10^{6} \pm 9.73 \times 10^{1}$
	Blood	$2.49 \times 10^{2} \pm 2.63 \times 10^{-2}$	44.17 ± 0.004	$1.99 \times 10^{3} \pm 1.57 \times 10^{-1}$
Immunocompromised	Lungs	$1.02 \times 10^{10} \pm 5.36 \times 10^{7}$	N/A	$9.58 \times 10^{10} \pm 4.57 \times 10^{8}$
	Spleen	$9.61 \times 10^{10} \pm 5.04 \times 10^{7}$	N/A	$9.04 \times 10^{11} \pm 4.29 \times 10^{9}$
	Liver	$6.76 \times 10^{11} \pm 3.48 \times 10^{9}$	N/A	$6.36 \times 10^{12} \pm 2.96 \times 10^{10}$
	Blood	$3.39 \times 10^{9} \pm 1.78 \times 10^{7}$	N/A	$3.19 \times 10^{10} \pm 1.52 \times 10^{8}$
Antibiotic + immunocompromised	Lungs	$2.48 \times 10^{4} \pm 5.71 \times 10^{-10}$	60.76 ± 0.02	$1.49 \times 10^{5} \pm 6.44 \times 10^{1}$
	Spleen	$2.41 \times 10^{5} \pm 4.83 \times 10^{-9}$	74.41 ± 0.03	$1.44 \times 10^{6} \pm 5.87 \times 10^{2}$
	Liver	$1.66 \times 10^{4} \pm 5.26 \times 10^{-10}$	86.00 ± 0.03	$9.94 \times 10^{6} \pm 3.13 \times 10^{3}$
	Blood	$8.27 \times 10^{3} \pm 1.55 \times 10^{-10}$	54.17 ± 0.02	$4.96 \times 10^{4} \pm 2.15 \times 10^{1}$

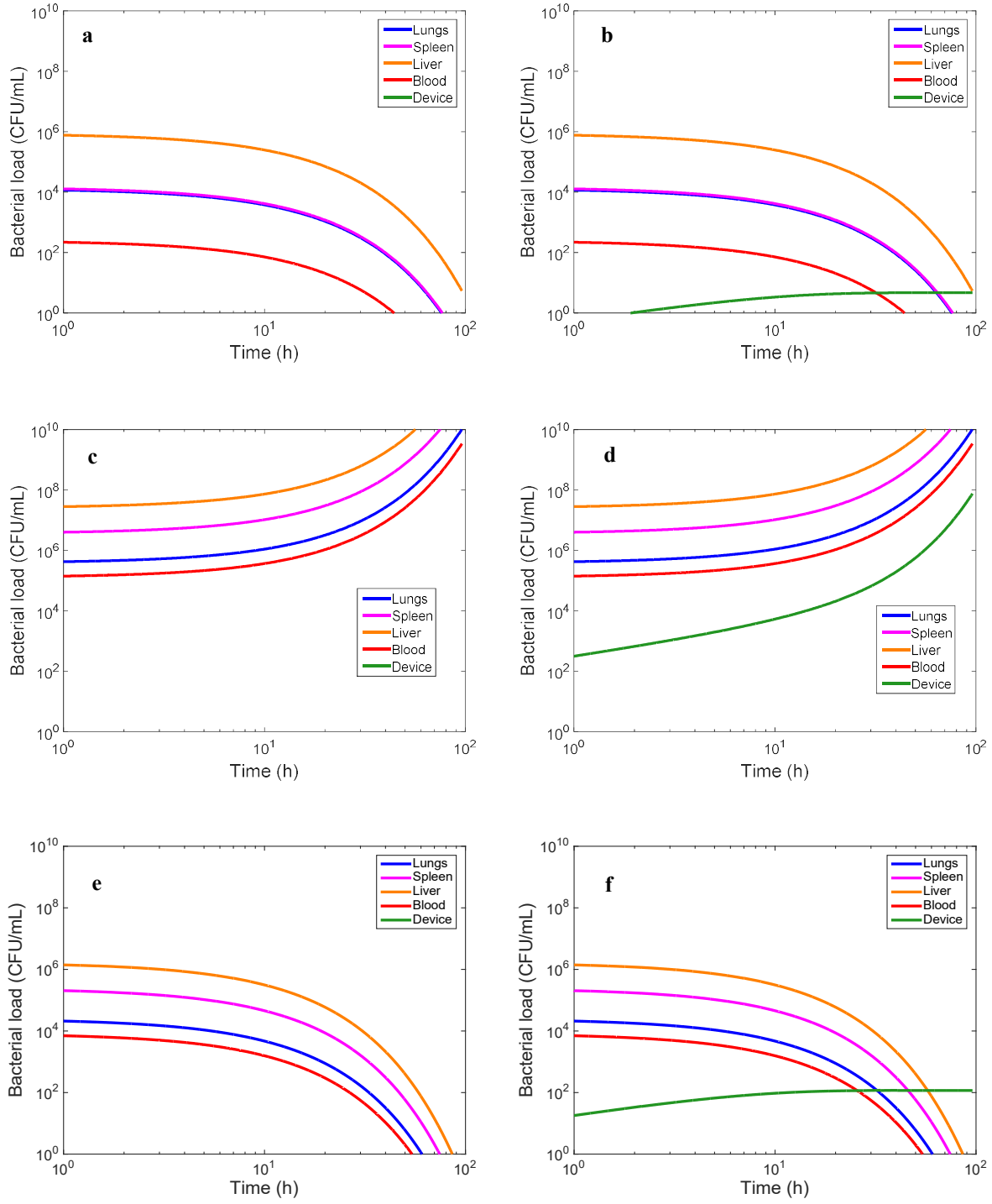

Figure 18: Log-log plots of bacterial load over time for all compartments with r_b = 75 nm and Q_E = 0.1 mL/min. From top to bottom: non-immunocompromised (a, b), immunocompromised (c, d), and immunocompromised with antibiotic (e, f). Left (a,c,e): without device separation; right (b,d,f): with device separation.

5.4. Conclusion

Incorporating a physically-based magnetic separation efficiency model into a physiologically-based pharmacokinetic model allows for a better understanding of the efficacy of a magnetics-based extracorporeal separation device. Using the model and parameters outlined, clinical outcomes would most likely not improve, since bacterial load metrics were not significantly changed by magnetic separation of bacteria from blood under any microsphere radius or device flow rate evaluated. High-throughput, high-capture devices will be essential for there to be any improvement of patient outcomes. Applying constrained nonlinear optimization to this problem with additional variables, such as device height and length, could better inform design by reducing the computational burden in exploring the feasible parameter space.

CHAPTER 6

Conclusions and future directions

Bacteremia and bacterial sepsis are a major public health concern due to the increasing number of cases of antibiotic resistance, rendering conventional treatment methods ineffective. To combat this emergence, the challenges of rapid diagnosis and treatment must be met. Extracorporeal bacterial separation methods show promise as a means to identify pathogens and cleanse blood of bacteria, reducing the overall bacterial load. Micromagnetic separation utilizes paramagnetic microparticles to transport bound bacteria from a primary fluid flow to a secondary sheath flow. To enable efficient separation of these particles, microfluidics must be used.

In this work, microfluidic devices for magnetic separation were fabricated using SU-8 photolithography and soft lithography and then characterized using volumetric flow measurements. These results were confirmed using computational fluid dynamics, which also improved understanding of the flow behavior within the devices. Additional modeling of micromagnetic separation using magnetostatic finite element analysis and a physiologically-based pharmacokinetic model provided further information for design considerations.

Based on the results of the mathematical modeling, a single device is insufficient to impact clinical outcomes in patients with bacteremia. Although bacteria could be removed via magnetic separation, the throughput and capacity of a device must be enough to impact the course of bacteremia in large living systems such as humans. Parallelization of several magnetic separation devices could potentially achieve the necessary thresholds; however, this drastically increases the complexity of the separation. Magnetic fields between devices would interact, potentially disrupting the consistent gradient observed in the two-magnet setup. Additionally,

flowing blood through microfluidic channels increases cellular activity and risks coagulation. Furthermore, any uncaptured magnetic microparticles would return to the patient, prompting toxicity concerns. Although micromagnetic separation has the potential to be a method of extracorporeal bacterial separation, many challenges must be overcome. Nevertheless, micromagnetic separation may be useful in diagnostic methods, since binding of specific and relevant moieties can be engineered for particles.

Appendix A: Infection model Matlab code

```
% Measured in CFU/m^3
c_0_in = 1e7 / 1e-6;

% Must use SI units (m, s, etc.)
w = 100e-6;
h = 100e-6;
n = 20000;
Q = 1.667e-8*[0.01:0.01:0.1,0.2:0.1:1.5];
l = 0.025;
a = w * h; % cross sectional area of a single channel of device

% Binding kinetics
b_500 = 0.0025; % concentration of 500nm magnetic particles (kg/m^3)

r_b = (25:5:500)*10^-9;

r_c = 0.5 * 10^-6; % spherical radius of A. baumannii bacteria (m)

b = b_500*(((5*10^-7)./r_b).^3); %b = concentration of magnetic beads. 5*10^-
7 m = nm to m = control bead radius

k_B = 1.38*10^-23; %Boltzmann's constant in kg*m^2*s^-2*K^-1

T = 300; %temperature in kelvin

n_b = 4 * (10^-3); %viscosity of blood in <N*s*m^-2>

%k_d = collision rate constant of diffusion

k_d_b = (2 * r_c * k_B * T)./(3 * n_b .* r_b); %blood

r_t = 0.005; % radius of 1.5 mL centrifuge tube (m)

Q_shear = 1e-7; %approximate volumetric flow rate  (m^3/s) in tube

gamma = (4 * Q_shear)/(pi * (r_t^3));

%k_shear = collision rate constant of shear

k_shear = pi * gamma .* (r_b + r_c).^3;


p = 0.5; %fraction of bacteria surface area that can be covered by NPs

N = 4 * p * ((r_c./r_b).^2); % N = number of NPs boud to single bacteria

delB2 = 4.7; %B = magnetic field intensity in <T^2/m>

x_v = 3.5; %Volumetric susceptibility of NPs
```

```
u_o = (4 * pi) * 10^-7; %magnetic permeability of a vacuum in <T*m*(A^-1)>

r_n = ((r_c.^3) + N .* (r_b.^3)).^(1/3); % Effective hydraulic radius

%v_mag = magnetophoretic velocity of bacteria labeled with magnetic NPs (m/s)

v_mag_n = ((r_b.^3) .* N .* x_v .* delB2)./(9 * r_n * n_b * u_o); % blood
v_mag_b = ((r_b.^2) .* x_v .* delB2)./(9 * n_b * u_o);

t_mag_n = w./v_mag_n; % bound bacteria
t_mag_b = w./v_mag_b; % beads only

t_2 = 5*60; % incubation time in seconds
c_e_b = 3.7e-4;
c_o_b = (c_0_in) .* exp(-1 * c_e_b * (k_d_b + k_shear) .* b .* t_2);%blood

h_n = zeros(length(Q),length(r_b));
g_n = zeros(length(Q),length(r_b));
g_b = zeros(length(Q),length(r_b));
f_b = zeros(length(Q),length(r_b));

thresh = 1; % CFU/mL

Lend = zeros(length(Q),length(r_b));
Send = zeros(length(Q),length(r_b));
Hend = zeros(length(Q),length(r_b));
Bend = zeros(length(Q),length(r_b));
Eend = zeros(length(Q),length(r_b));

Lmax = zeros(length(Q),length(r_b));
Smax = zeros(length(Q),length(r_b));
Hmax = zeros(length(Q),length(r_b));
Bmax = zeros(length(Q),length(r_b));
Emax = zeros(length(Q),length(r_b));

LAUC = zeros(length(Q),length(r_b));
SAUC = zeros(length(Q),length(r_b));
HAUC = zeros(length(Q),length(r_b));
BAUC = zeros(length(Q),length(r_b));
EAUC = zeros(length(Q),length(r_b));

Lthresh = zeros(length(Q),length(r_b));
Sthresh = zeros(length(Q),length(r_b));
Hthresh = zeros(length(Q),length(r_b));
Bthresh = zeros(length(Q),length(r_b));

status = 1;

t_i = 10;
[t0,y0] = ode45(@(t,y) KP_Human_infection_model_v2(t,y,[0 w h n l status
0]),[0 t_i],[c_0_in/1e6 0 0 0 0]);
y00 = y0(end,:); % Bacteria levels ten hours after inoculation

t_h = 96; % hours of treatment
```

```
for j = 1:length(Q)
    %v_l = linear average velocity of bacteria labeled with MNPs flowing

    %through 1 of the n channels of the device (m/s)

    v_l = Q(j)/(n * a);

    %t_res = characteristic residence time in a channel (s)

    t_res = l/v_l;

    %t_mag = time required for the complex to magnetically migrate from

    %position A to position B (s)

    for k = 1:length(r_b)
        if (t_res >= t_mag_n(k))
            g_n(j,k) = 1;
            h_n(j,k) = (1 - exp(-c_e_b * (k_d_b(k) + k_shear(k)) .* b(k) .*
c_o_b(k) .* t_2));
            f_b(j,k) = h_n(j,k);
        elseif (t_res < t_mag_n(k))
            g_n(j,k) = t_res/t_mag_n(k);
            h_n(j,k) = (t_res .* ((1 - exp(-c_e_b * (k_d_b(k) + k_shear(k))
.* b(k) .* c_o_b(k) .* t_2)))) ./t_mag_n(k);
            f_b(j,k) = h_n(j,k)/g_n(j,k);
        end
    end

    g_b(j,:) = t_res./t_mag_b;

    parfor (k = 1:length(r_n), 4)
        [j,k]
        f = h_n(j,k); % fraction of bacteria captured
        [tjk,yjk] = ode45(@(t,y) KP_Human_infection_model_v2(t,y,[Q(j) w h n
l status f]),[0 t_h],y00);

        Lend(j,k) = yjk(end,1);
        Send(j,k) = yjk(end,2);
        Hend(j,k) = yjk(end,3);
        Bend(j,k) = yjk(end,4);
        Eend(j,k) = yjk(end,5);

        Lmax(j,k) = max(yjk(:,1));
        Smax(j,k) = max(yjk(:,2));
        Hmax(j,k) = max(yjk(:,3));
        Bmax(j,k) = max(yjk(:,4));
        Emax(j,k) = max(yjk(:,5));

        LAUC(j,k) = trapz(tjk,yjk(:,1));
        SAUC(j,k) = trapz(tjk,yjk(:,2));
        HAUC(j,k) = trapz(tjk,yjk(:,3));
        BAUC(j,k) = trapz(tjk,yjk(:,4));
        EAUC(j,k) = trapz(tjk,yjk(:,5));
```

```
        if size(find(yjk(:,1)<=thresh),1) ~= 0
            Lthresh(j,k) = tjk(find(yjk(:,1)<=thresh,1));
        end
        if size(find(yjk(:,2)<=thresh),1) ~= 0
            Sthresh(j,k) = tjk(find(yjk(:,2)<=thresh,1));
        end
        if size(find(yjk(:,3)<=thresh),1) ~= 0
            Hthresh(j,k) = tjk(find(yjk(:,3)<=thresh,1));
        end
        if size(find(yjk(:,4)<=thresh),1) ~= 0
            Bthresh(j,k) = tjk(find(yjk(:,4)<=thresh,1));
        end
    end
end

figure(1);
plot(r_b,f_b(1,:));
title('Binding efficiency');
figure(2);
surf(r_b,Q/1.667e-8,g_n);
title('Magnetic separation efficiency of complexes');
figure(3);
surf(r_b,Q/1.667e-8,h_n);
title('Overall separation efficiency');
figure(4);
surf(r_b,Q/1.667e-8,g_b);
title('Magnetic separation of microspheres');

figure(5);
surf(r_b,Q/1.667e-8,Lend);
title('Bacterial load in lungs after treatment');
figure(6);
surf(r_b,Q/1.667e-8,Send);
title('Bacterial load in spleen after treatment');
figure(7);
surf(r_b,Q/1.667e-8,Hend);
title('Bacterial load in liver after treatment');
figure(8);
surf(r_b,Q/1.667e-8,Bend);
title('Bacterial load in blood after treatment');
figure(9);
surf(r_b,Q/1.667e-8,Eend);
title('Bacterial load in device after treatment');

figure(10);
surf(r_b,Q/1.667e-8,Lmax);
title('Maximum bacterial load in lungs');
figure(11);
surf(r_b,Q/1.667e-8,Smax);
title('Maximum bacterial load in spleen');
figure(12);
surf(r_b,Q/1.667e-8,Hmax);
title('Maximum bacterial load in liver');
figure(13);
surf(r_b,Q/1.667e-8,Bmax);
```

```
title('Maximum bacterial load in blood');
figure(14);
surf(r_b,Q/1.667e-8,Emax);
title('Maximum bacterial load in device');

figure(15);
surf(r_b,Q/1.667e-8,Lthresh);
title('Time to threshold in lungs');
figure(16);
surf(r_b,Q/1.667e-8,Sthresh);
title('Time to threshold in spleen');
figure(17);
surf(r_b,Q/1.667e-8,Hthresh);
title('Time to threshold in liver');
figure(18);
surf(r_b,Q/1.667e-8,Bthresh);
title('Time to threshold in blood');

[t1,y1] = ode45(@(t,y) KP_Human_infection_model_v2(t,y,[0 w h n l status
0]),[0 t_h],y00);
figure(19);
loglog(t1,y1(:,1),'b','LineWidth',3);
hold on;
loglog(t1,y1(:,2),'Color',[1 0 1],'LineWidth',3);
loglog(t1,y1(:,3),'Color',[1 0.5 0],'LineWidth',3);
loglog(t1,y1(:,4),'r','LineWidth',3);
loglog(t1,y1(:,5),'Color',[34 149 34]/255,'LineWidth',3);
hold off;
xlim([1 100]);
ylim([1 1e10]);
xlabel('Time (h)','FontSize',22);
ylabel('Bacterial load (CFU/mL)','FontSize',22);

[t2,y2] = ode45(@(t,y) KP_Human_infection_model_v2(t,y,[Q(10) w h n l status
h_n(11,10)]),[0 t_h],y00);
figure(20);
loglog(t2,y2(:,1),'b','LineWidth',3);
hold on;
loglog(t2,y2(:,2),'Color',[1 0 1],'LineWidth',3);
loglog(t2,y2(:,3),'Color',[1 0.5 0],'LineWidth',3);
loglog(t2,y2(:,4),'r','LineWidth',3);
loglog(t2,y2(:,5),'Color',[34 149 34]/255,'LineWidth',3);
hold off;
xlim([1 100]);
ylim([1 1e10]);
xlabel('Time (h)','FontSize',22);
ylabel('Bacterial load (CFU/mL)','FontSize',22);
```

Appendix B: PBPK differential equations Matlab function

```
 function dydt = KP_Human_infection_model_v2(t,y,PARAM) %#ok<INUSL>
% PARAM(1) = total flow rate through device
% PARAM(2) = channel width
% PARAM(3) = channel height
% PARAM(4) = number of channels
% PARAM(5) = channel length
% PARAM(6) = immuno status
% PARAM(7) = fractional separation

% L = lung
% S = spleen
% H = liver
% B = blood
% E = extracorpoeral device

Q_E = PARAM(1)*3600; % conversion to m^3/h
w = PARAM(2);
h = PARAM(3);
n = PARAM(4);
l = PARAM(5);

% Growth rate (1/h)
if PARAM(6) == 0 % immunocompromised
    G_L = 0.21;
    G_S = 0.14;
    G_H = 0.10;
    G_B = 0.08;
elseif PARAM(6) == 1 % immunocompromised with antibiotic
    G_L = -0.24;
    G_S = -0.07;
    G_H = -0.18;
    G_B = -0.05;
elseif PARAM(6) == 2 % non-immunocompromised
    G_L = -1.74;
    G_S = -0.14;
    G_H = -0.10;
    G_B = -0.17;
end

%V = blood volume (m^3)

V_L = 450e-6;

V_S = 2.09e-4;

V_H = 0.00156; % 9 percent of total blood volume

V_E = n * w * h * l;

%Q = rate of blood flow to each compartment (m^3/h)

Q_L = 0.08995;
```

```
Q_S = 0.01501;

Q_H = 0.0483;

% Partition coefficients (dimless)
if PARAM(6) == 0 || PARAM(6) == 1
    p_L = 3;
    p_S = 28;
    p_H = 79;
elseif PARAM(6) == 2
    p_L = 93;
    p_S = 59;
    p_H = 749;
end


% magnetic separation

L = y(1);

S = y(2);

H = y(3);

B = y(4);

E = y(5);

f = PARAM(7);

% magnetic separation

dydt = zeros(size(y));

dydt(1) = (G_L*L) + ((Q_L/V_L)*B) - ((Q_L/(V_L*p_L))*L);

dydt(2) = (G_S*S) + ((Q_S/V_S)*B) - ((Q_S/(V_S*p_S))*S);

dydt(3) = (G_H*H) + ((Q_H/V_H)*B) + ((Q_S/(V_S*p_S))*S) -
(((Q_H+Q_S)/(V_H*p_H))*H);

dydt(4) = (G_B*B) + (((Q_H+Q_S)/(V_H*p_H))*H) + ((Q_L/(V_L*p_L))*L) -
(((Q_H/V_H) + (Q_S/V_S) + (Q_L/V_L)+ (f * (Q_E/V_E)))*B);

dydt(5) = ((Q_E/(V_E)) .* B .* f);
```

REFERENCES

[1] C. W. Seymour *et al.*, "Assessment of Clinical Criteria for Sepsis: For the Third International Consensus Definitions for Sepsis and Septic Shock (Sepsis-3).," *Jama*, vol. 315, no. 8, pp. 762–74, 2016.

[2] I. László, D. Trásy, Z. Molnár, and J. Fazakas, "Sepsis : From Pathophysiology to Individualized Patient Care," vol. 2015, 2015.

[3] J. L. Vincent, S. M. Opal, J. C. Marshall, and K. J. Tracey, "Sepsis definitions: Time for change," *Lancet*, vol. 381, no. 9868, pp. 774–775, 2013.

[4] F. W. Guirgis *et al.*, "The long-term burden of severe sepsis and septic shock," *J. Trauma Acute Care Surg.*, vol. 81, no. 3, p. 1, 2016.

[5] T. J. Iwashyna, E. W. Ely, D. M. Smith, and K. M. Langa, "Long-term Cognitive Impairment and Functional Disability Among Survivors of Severe Sepsis," *Jama-Journal Am. Med. Assoc.*, vol. 304, no. 16, pp. 1787–1794, 2010.

[6] M. J. Hall, S. N. Williams, C. J. DeFrances, and A. Golosinskiy, "Inpatient care for septicemia or sepsis: a challenge for patients and hospitals.," *NCHS Data Brief*, no. 62, pp. 1–8, 2011.

[7] D. C. Angus, W. T. Linde-Zwirble, J. Lidicker, G. Clermont, J. Carcillo, and M. R. Pinsky, "Epidemiology of severe sepsis in the United States: analysis of incidence, outcome, and associated costs of care.," *Crit. Care Med.*, vol. 29, no. 7, pp. 1303–1310, 2001.

[8] G. S. Martin, "Sepsis, severe sepsis and septic shock: changes in incidence, pathogens and outcomes," *Expert Rev Anti Infect Ther*, vol. 10, no. 6, pp. 701–706, 2012.

[9] NIGMS, "Sepsis Fact Sheet," 2017. [Online]. Available:

http://www.cdc.gov/sepsis/pdfs/sepsis-fact-sheet.pdf. [Accessed: 04-Mar-2017].

[10] F. B. Mayr, S. Yende, and D. C. Angus, "Epidemiology of severe sepsis.," *Virulence*, vol. 5, no. 1, pp. 4–11, 2014.

[11] J. D. Faix, "Biomarkers of sepsis," vol. 8363, no. 1, pp. 23–36, 2013.

[12] J. L. Vincent, "The Clinical Challenge of Sepsis Identification and Monitoring," *PLoS Med.*, vol. 13, no. 5, pp. 1–10, 2016.

[13] S. L. Raymond, J. A. Stortz, J. C. Mira, S. D. Larson, and J. L. Wynn, "Immunological Defects in Neonatal Sepsis and Potential Therapeutic Approaches," vol. 5, no. February, pp. 1–8, 2017.

[14] K. Chun *et al.*, "Sepsis Pathogen Identification," 2015.

[15] K. Yuki and N. Murakami, "Sepsis pathophysiology and anesthetic consideration.," *Cardiovasc. Hematol. Disord. Drug Targets*, vol. 15, no. 1, pp. 57–69, 2015.

[16] S. E. Miller, C. S. Bell, M. S. Mcclain, T. L. Cover, and T. D. Giorgio, "Dynamic Computational Model of Symptomatic Bacteremia to Inform Bacterial Separation Treatment Requirements," *PLoS One*, vol. 11, no. 9, pp. 1–22, 2016.

[17] R. S. Munford, "SEVERE SEPSIS AND SEPTIC SHOCK: The Role of Gram-Negative Bacteremia," *Annu. Rev. Pathol. Mech. Dis.*, vol. 1, no. 1, pp. 467–496, 2006.

[18] O. Cirioni *et al.*, "Therapeutic efficacy of buforin II and rifampin in a rat model of Acinetobacter baumannii sepsis," *Crit. Care Med.*, vol. 37, no. 4, pp. 1403–1407, 2009.

[19] A. Kumar *et al.*, "Duration of hypotension before initiation of effective antimicrobial therapy is the critical determinant of survival in human septic shock," *Crit Care Med.*, vol. 34, no. 0090–3493 (Print), pp. 1589–1596, 2006.

[20] A. Langdon, N. Crook, and G. Dantas, "The effects of antibiotics on the microbiome

throughout development and alternative approaches for therapeutic modulation.," *Genome Med.*, vol. 8, no. 1, p. 39, 2016.

[21] J. Tanwar, S. Das, Z. Fatima, and S. Hameed, "Multidrug resistance: An emerging crisis," *Interdiscip. Perspect. Infect. Dis.*, vol. 2014, 2014.

[22] CDC, "Antibiotic resistance threats in the United States, 2013," *Current*, p. 114, 2013.

[23] World Health Organization, "The evolving threat of antimicrobial resistance: Options for action," *WHO Publ.*, pp. 1–119, 2014.

[24] E. Bergogne-Bérézin and K. J. Towner, "Acinetobacter spp. as nosocomial pathogens: Microbiological, clinical, and epidemiological features," *Clin. Microbiol. Rev.*, vol. 9, no. 2, pp. 148–165, 1996.

[25] A. Howard, M. O'Donoghue, A. Feeney, and R. D. Sleator, "Acinetobacter baumannii: an emerging opportunistic pathogen.," *Virulence*, vol. 3, no. 3, pp. 243–50, 2012.

[26] P. E. Fournier, "The Epidemiology and Control of Acinetobacter baumannii in Health Care Facilities HABITAT," vol. 42, 2006.

[27] A. Abbo, S. Navon-Venezia, O. Hammer-Muntz, T. Krichali, Y. Siegman-Igra, and Y. Carmeli, "Multidrug-resistant Acinetobacter baumannii," *Emerg. Infect. Dis.*, vol. 11, no. 1, pp. 22–29, 2005.

[28] J. Y. Choi *et al.*, "Mortality risk factors of Acinetobacter baumannii bacteraemia," pp. 599–603, 2005.

[29] M. Paul *et al.*, "Acinetobacter baumannii: Emergence and spread in Israeli hospitals 1997-2002," *J. Hosp. Infect.*, vol. 60, no. 3, pp. 256–260, 2005.

[30] T. Chopra *et al.*, "Epidemiology of Bloodstream Infections Caused by Acinetobacter baumannii and Impact of Drug Resistance to both Carbapenems and Ampicillin-

Sulbactam on Clinical Outcomes," vol. 57, no. 12, pp. 6270–6275, 2013.

[31] S. Gupta *et al.*, "Colistin and polymyxin B: A re-emergence," *Indian J. Crit. Care Med.*, vol. 13, no. 2, p. 49, Nov. 2009.

[32] J. Li *et al.*, "Colistin: the re-emerging antibiotic for multidrug-resistant Gram-negative bacterial infections," *Lancet Infect. Dis.*, vol. 6, no. 9, pp. 589–601, 2006.

[33] J. H. Kang, S. Krause, H. Tobin, A. Mammoto, M. Kanapathipillai, and D. E. Ingber, "A combined micromagnetic-microfluidic device for rapid capture and culture of rare circulating tumor cells," *Lab Chip*, vol. 12, no. 12, p. 2175, 2012.

[34] W. Lee, D. Kwon, W. Choi, G. Y. Jung, and S. Jeon, "3D-printed microfluidic device for the detection of pathogenic bacteria using size-based separation in helical channel with trapezoid cross-section.," *Sci. Rep.*, vol. 5, p. 7717, 2015.

[35] N. Xia *et al.*, "Combined microfluidic-micromagnetic separation of living cells in continuous flow," *Biomed. Microdevices*, vol. 8, no. 4, pp. 299–308, 2006.

[36] C. W. Yung, J. Fiering, A. J. Mueller, and D. E. Ingber, "Micromagnetic-microfluidic blood cleansing device," *Lab Chip.*, vol. 9, no. 1473–0197 (Print), pp. 1171–1177, 2009.

[37] J. H. Kang *et al.*, "An extracorporeal blood-cleansing device for sepsis therapy," *Nat. Med.*, vol. 20, no. 10, pp. 1211–1216, 2014.

[38] J. H. Kang *et al.*, "Optimization of Pathogen Capture in Flowing Fluids with Magnetic Nanoparticles," *Small*, vol. 11, no. 42, pp. 5657–5666, 2015.

[39] C. C. Marasco, J. R. Enders, K. T. Seale, J. A. McLean, and J. P. Wikswo, "Real-time cellular exometabolome analysis with a microfluidic-mass spectrometry platform," *PLoS One*, vol. 10, no. 2, pp. 1–19, 2015.

[40] J. Jung and A. Hassanein, "Three-phase CFD analytical modeling of blood flow," *Med.*

Eng. Phys., vol. 30, no. 1, pp. 91–103, 2008.

[41] K. Magnetics, "K&J Magnetics - Magnetic Field Visualization (BX04X0)." [Online]. Available: https://www.kjmagnetics.com/magfield.asp?pName=BX04X0. [Accessed: 20-Mar-2017].

[42] B. Cheewatrakoolpong, E. K. Steffen, R. Don Brown, and R. D. Berg, "Kinetic analysis of bacterial clearance in mice using the ESTRIPc and KINET microcomputer programs," *J. Immunol. Methods*, vol. 58, no. 3, pp. 375–381, 1983.

[43] W. Dzwinel, K. Boryczko, and D. A. Yuen, "A discrete-particle model of blood dynamics in capillary vessels," *J. Colloid Interface Sci.*, vol. 258, no. 1, pp. 163–173, 2003.